Results in Physics 66 (2024) 108022

Contents lists available at ScienceDirect

Results in Physics

journal homepage: www.elsevier.com/locate/rinp

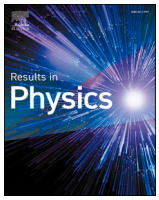

Theoretical investigations on exploring Si-based heterostructures with cubic and ground-state perovskites

Yunting Liang [a,*], Yajun Zhang [b], Wenyi Tong [c], Philippe Ghosez [c], Eric Bousquet [c], Matjaž Spreitzer [d]

[a] School of Energy Engineering, Huanghuai University, Zhumadian 463000, China
[b] Key Laboratory of Mechanics on Disaster and Environment in Western China, Ministry of Education of China, Lanzhou University, Lanzhou 730000, China
[c] Theoretical Materials Physics, Q-MAT, CESAM, University of Liège, B-4000 Liège, Belgium
[d] Advanced Materials Department, Jožef Stefan Institute, Jamova 39, 1000 Ljubljana, Slovenia

A B S T R A C T

First principles calculations in the framework of density functional theory (DFT) are performed to exploit replaceable perovskite oxides against the instability of traditional cubic $SrTiO_3$ grown on silicon substrate. In this work, we consider more thermostable $CaTiO_3$ and $CaZrO_3$ with cubic and ground-state phase as the candidates to perform the gate dielectric. After the calibration of total energy and lattice transformation of ground-state perovskites to match with Si substrate, three categories of 2×2 heterostructures have been constructed and investigated through the geometrical change, atom displacement around interfacial layer, total energy and electronic structure change, under the variations on perovskite species, the concentration of interfacial layer and the thickness of perovskite film. And the results demonstrate that the category with half a monolayer of Ca/Sr atoms in interfacial layer and two unit-cell perovskite thicknesses show the type-I band alignment through their band alignment. Among this category, the heterostructure with Pnma $CaZrO_3$ shows semiconductivity and excellent electrical property with larger band offset for the candidate of gate dielectric. This work provides a creative perspective to expand the perovskite diversity for the booming growth of integrated circuit technology.

Introduction

Since the integrated circuit set sail from 1959, the electronic technology had started to utilize silica (SiO_2) treated as the gate dielectric material in a field effect transistor. However, the transistor technology relied on silica is facing the fundamental limit problem. Due to silica thickness leading to excessive tunneling currents and further making transistor design indefensible, so the feature-size reduction as the ever-demanding transistor technology have set up scaling restraints on the thickness of gate oxide, and an optimal substitution on traditional gate dielectric is urgently demanded [1]. Besides, many works have been conducted from different perspectives for decades, aiming to improve exponentially the speed and density of transistors against an observationn called as Moore's law with upgrading in roughly every 18 months [2–5].

The complementary metal–oxide–semiconductor (CMOS) integrated circuit technology just fulfills the requirement of the continuous-scaling target in micro-electronic devices by replacing silica with new high k materials [6,7]. The integration of complex transition metal oxides on semiconductor platforms inspires the great interests to relevant researchers. Different from silica, since it realizes the entire functional enrichment through the coupling properties between the transition metal oxide film and silicon substrate, which would enable the innovative creation of electronic devices [8].

Since the first realization of epitaxial growth of cubic $SrTiO_3$ (STO) on Si with an equivalent oxide thickness $t_{eq} < 10$ Å by McKee *et al.* [9], STO becomes one of the most promising substitutions due to $SrTiO_3$ possessing ~200 dielectric constant, which has been widely studied through experimentally and theoretically [10,11]. Among them, Kolpak et al[12] have carried out sufficiently and systematically theoretical investigations on cubic $SrTiO_3$ with Si(001), including the interface compositions and geometries, the atomic and electronic structures of heterostructures, and the band alignments of heterostructures. Their works provide an overall perspective of geometries and properties of $SrTiO_3$/Si(001) for the future design of coupled functional oxide–semiconductor devices.

However, it reported that $SrTiO_3$ materials are not stable in direct contact with silicon at 920 °C [13]. The thermal stability of high k dielectric on silicon is an important factor for future MOSFET devices, since the gate dielectric must tolerate a high temperature around 900 °C

* Corresponding author.
E-mail address: ytliang@huanghuai.edu.cn (Y. Liang).

https://doi.org/10.1016/j.rinp.2024.108022
Received 20 June 2024; Received in revised form 27 September 2024; Accepted 21 October 2024
Available online 22 October 2024

for short time in standard MOSFET processing [14]. Therefore, it demands to consider other perovskite oxides with high thermal stability. Very surprisingly, $CaTiO_3$ and $CaZrO_3$ are estimated with high-temperature thermal stability around 1300 K and high k value ($CaTiO_3 \sim 180$; $CaZrO_3 \sim 30$) [15,16], meanwhile $CaZrO_3$ has been confirmed stable under low Si-activity conditions [17]. Besides, Hubbard and Schlom [18] have studied the stability of several binary metal oxides in contact with silicon at 1000 K, they demonstrate that CaO, ZrO_2, TiO_2 and MgO are thermodynamically stable, and these binary metal oxides could exist as the direct contact layer of perovskite oxides integrated with silicon substrates.

Additionally, including the cubic phase of new candidates $CaTiO_3$ and $CaZrO_3$, their ground-state phases are also worth to investigate. Since the room-temperature phase of $SrTiO_3$ is cubic Pm $\bar{3}$ m [19], elated theoretical researches around it all adopt this symmetry to simulate the actual application, for the purpose to close to experimental results. Similarly, $CaTiO_3$ and $CaZrO_3$ show the consistent symmetry with orthorhombic phase in room temperature and ground state, Pnma space group [20,21]. Interestingly, the matching of ground-state structures with oxygen octahedron distortion and silicon substrates is rarely studied, how these oxygen octahedrons in perovskite films deform and affect the entire electronic properties would be worth to launch [22].

Here cubic and tetragonal $SrTiO_3$ are also added for the comparison. The paper is organized as follows. In Section 2, we introduce the technical details of our DFT calculations. Then in Section 3, we address separately three parts to discuss the bulk transformation, three types of heterostructures with different perovskites film and their electronic properties and their band alignments. Finally, an overall conclusion is made to review the whole study.

Methods

The calculations were implemented through the density-functional theory (DFT) [23,24], by employing the full-potential projector augmented wave (PAW) method for ionic potentials [25], as carried out in the Vienna ab initio Simulation Package, VASP (v5.3.3) [26]. Here we used the PBEsol functional as the exchange–correlation potential in the framework of generalized gradient approximation (GGA) for efficient structure-energy modelling to determine the stable structures after relaxation [27]. A kinetic energy cut-off of 600 eV was adopted, and Monkhorst-Pack k-point mesh (firstly introduced by Monkhorst [28]) was defined with spacing below 0.03 $Å^{-1}$ for structure-energy calculation, a finer K mesh was chosen for electronic structures with spacing below 0.04 $Å^{-1}$. The convergence criterion for the self-consistent energy was 10^{-6} eV and the geometrical structures were relaxed until the Hellmann–Feynman residual forces below 10 meVnm^{-1}. We took the electronic configurations into account with their valence electrons and pseudopotential versions as follow: Si($3s^2 3p^2$, v-05Jan2001), Ca($3s^2 3p^6 4s^2$, 06Sep2000), Sr($4s^2 4p^6 5s^2$, v-07Sep2000), H(1 s^1, v-15Jun2001), Ti($3d^2 4s^2$, v-08Apr2002), Zr($4s^2 4p^6 5s^2 4d^2$, 04Jan2005) and O($2s^2 2p^4$, v-08Apr2002). The perovskite/Si (001) surfaces were modelled by adopting a slab geometry. The chosen simulation substrate was composed of five silicon layers, in agreement with others [29,30]. A large 3 × 3 supercell with nine Si atoms in the top atomic layer of Si substrate was adopted to make the relevant calculations. The Si dangling bonds in the vacuum-exposed Si surface at the slab bottom were passivated with hydrogen atoms in order to facilitate the simulation of a thick Si substrate. To avoid the spurious slab-slab interactions, we considered that a vacuum region of at least 1.5 nm was included between the repeated slabs, and a dipole correction was added in this calculation [12,31].

Based on the modeling simulation of traditional $SrTiO_3$/Si slab the in-plane symmetry of the supercell (2 × 1) for most previous calculations [12], here (2 × 2) in-plane symmetry in this study was performed for six kinds of perovskite films ($CaTiO_3$, $CaZrO_3$ and $SrTiO_3$, and their cubic and ground-state phase), especially for ground-state perovskite to minimally exhibit octahedral rotations or tilting patterns in the perovskite film. Normally, the epitaxial growth of $SrTiO_3$/Si firstly required the initial deposition of half a monolayer (ML) of Sr atoms on Si substrate, in the purpose of the charge compensation nominally on the Si dangling bonds at the dimerized surface of the silicon substrate, to avoid the formation of an amorphous silica layer occurred at the $SrTiO_3$/Si interface [9,32–34]. Therefore in this study, the interfacial layer (IFL) adjacent to both full atomic layers of silicon and perovskite film, was varied same with the composition of alkaline-earth metal in perovskites (e.g. Ca IFL in $CaTiO_3$), considering for the experimental deposition.

To obtain band alignments of these heterostructures, we employed an electrostatic potential-based alignment method to get the valence and conduction band offsets [35,36]. To realize the extraction of band alignment representative of an interface, firstly the preparation for thicker layers of each of two materials reached the minimum of eight atomic layers to get the macroscopic averaged electrostatic potential, then the utilization of the center part from the electrostatic potentials to simulate the bulk-like was necessary for the accurate calculation [37,38]. The valence band offset at the interface was calculated according to the equation $\Delta Ev = \Delta EP_{int} - \Delta EP + \Delta E_{VBM}$, where ΔEP_{int} is the internal potential across the interfaces, and ΔEP and ΔE_{VBM} refer to the differences between the electrostatic potential and the valence band edges of two independent bulk materials, respectively. Finally, the conduction band offsets (ΔEc) was calculated by counting the band gap of each material on ΔEv, here the band gap can be obtained by the experiment measurement or using hybrid exchange–correlation functional, like B3PW or B3LYP, which allows to achieve an excellent agreement with the experiment for the band gaps of the related perovskite oxide materials [39].

Results and discussion

Lattice transformation in bulk perovskites with ground states

In order to facilitate the integration of perovskite bulk and Si substrate, the energy reliability and lattice transformation of perovskite bulk need to be primarily investigated. We calculate total energies per formular unit (f.u.) of three perovskite bulks, to insure the accuracy of this simulation. After the comparison of total energies of these cubic and ground-state perovskites, the energies of Pnma $CaTiO_3$ and $CaZrO_3$ are respectively lower 0.338 eV and 0.963 eV than that of cubic phases. These results are in line with the basic rule of energy difference with the results from Dinela et al. [40], where the ground state of $CaTiO_3$ with Pnma structure is ≦-350 meV/f.u. below the cubic phase, and Pnma $CaZrO_3$ is lower by around −1.0 eV/f.u. than the P m$\bar{3}$m phase. From this perspective, it is reliable to carry out the further transformation works.

Subsequently, in order to select a suitable lattice plane to match with the silicon substrate, here we initially take orthorhombic $CaTiO_3$ (Pnma space group) as the target to perform the lattice transformation on its ground-state structure, immensely different from the direct match between cubic perovskite and Si. As shown in Fig. 1, Pnma $CaTiO_3$ with $\sqrt{2} \times \sqrt{2} \times 2$ primitive cell is firstly modified by matrix1 (110,1–10,001) into 2 × 2 × 2 supercell with ($a^- a^- c^+$) mode, then matrix2 (101,10–1,010) is adopted to realize the exchange of b-c axis into 2 × 2 × 2 supercell with ($a^- c^+ a^-$) mode, attempting to evaluate the priority of their energies for the best match with Si substrate.

Furthermore, we manage to fix their axial lengths on a and b directions by two times of Si lattice ($a = 3.84$ Å) in 2 × 2 × 2 transferred structures above, into two new-created structures (defined as CTO-AB and CTO-AC). This action is realized by the parameter settings in calculation software, and their c axes rotate randomly to achieve the lowest total energy, motivated by previous work called “strained bulk” calculation [41,42]. After the sufficient relaxation, their lowest energies

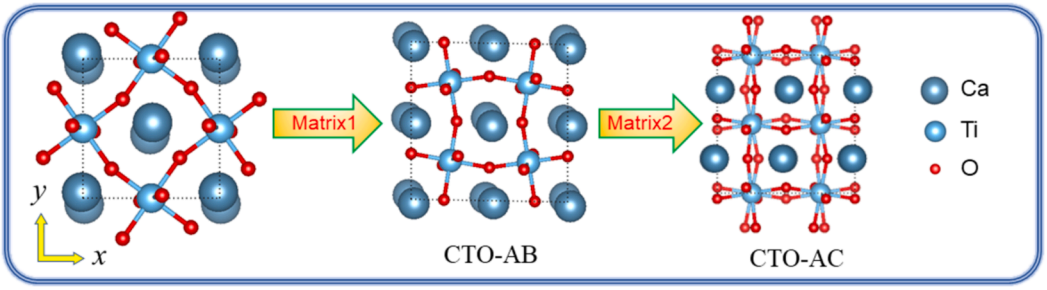

Fig. 1. (a) The transformation path of Pnma $CaTiO_3$ primitive cell through two matrixes.

and the corresponding lattice constants are obtained, as plotted in Fig. 2a. It can be concluded that the total energy of CTO-AC is slightly lower than that of CTO-AB, indicating that the arrangement of the crystal axes in this lattice is relatively stable. However, the c axis in CTO-AC structure cants with their ab plane, which goes against the well-growth deposition on Si substrate. Therefore, we limit its c axis perpendicular to the ab plane, to form a non-canted structure (called as non-canted CTO) to facilitate vertical growth on the silicon substrate. After that, the energy of this non-canted structure just slightly increase by 0.015 eV higher than that of original orthorhombic structure, favorable for the lattice match.

Similarly, we attempt to apply the lattice transformation method of Pnma $CaTiO_3$ into Pnma $CaZrO_3$ and I4/mcm $SrTiO_3$, and lattice parameters and total energy per f.u. are illustrated in the Fig. 2a. The total energy of the non-canted structure of $CaZrO_3$ (non-canted CZO) has increased enormously by 10.856 eV, while the energy of $SrTiO_3$ (non-canted STO) is inversely 0.021 eV lower than the initial structure. Here the larger $CaZrO_3$ bulk limited in 2 times of Si lattice causes the energy raise of non-canted CZO, but the obtained increscent innerstrain can also improve the polarization of its heterostructure simultaneously. Additionally, the decomposition of distortion model for all non-cubic structures in Fig. 2c reveals that the distortion amplitude of transferred $CaTiO_3$ is reasonably 0.028/Å lower than that of the parent Pnma structure, while the distortion degree of converted $CaZrO_3$ and $SrTiO_3$ increase by 0.052/Å and 0.073/Å compared with their parents.

Conclusively, we consider the lattice matching in all perovskites and Si(0 0 1) substrates. The in-plane lattice constants of all perovskites are fixed to the theoretical Si lattice constant ($a = 3.84$ Å) [43], convenient for the deposition on silicon substrate. This results in degrees of compressive strain in bulk perovskites, 0.1 % for cubic $CaTiO_3$ ($a = 3.844$ Å), 6.7 % for cubic $CaZrO_3$ ($a = 4.101$ Å), 1.7 % for cubic $SrTiO_3$ ($a = 3.908$ Å) and 0.07 % for three non-canted crystal structures, due to the aforehand lattice setting with 2 times of Si lattice constant for 2 × 2 × 2 supercell.

Three geometrical categories of (2 × 2) heterostructures

In this section, we introduce a representative subset of the perovskite/Si heterostructures and compositions to investigate the variation of geometrical and electronic structures. The minimum-energy atomic geometries computed for these compositions are showed in Fig. 3∼5. We examine the structural changes in the heterostructures with respect to three types of perturbation: (i) the variation in three types of perovskites: $CaTiO_3$, $CaZrO_3$ and $SrTiO_3$, and their cubic and ground-state phase, respectively; (ii) the change of composition and concentration in the interfacial layer: Ca/Sr, corresponding to their perovskite composition in A site; (iii) the change in the thickness of upper perovskite film, variant with two and four unit-cell layers. In particular, we examine these composition-induced changes in perovskite/Si heterostructures on the length of the Si dimer bonds (abbreviated as l_{dimer}) described in the illustration of Fig. 3, silicon-oxide separation ($d_{Si\text{-}oxide}$), the distance between interfacial layer and oxygen in first oxide layer of perovskite ($d_{Sr(Ca)\text{-}O}$), and the oxygen displacements in the perovskite layer adjacent to the interface (δ_{zint}). Knowledge of the variation in these parameters in relation to composition can be adopted in coordination with experimental data to confirm the interfacial atom geometry and composition for practical fabricated heterostructures [44].

(1) Geometrical feature of three categories

Firstly, two unit-cell perovskite film and half a monolayer (ML) of interfacial layer (IFL) are considered in (2 × 2) in-plane symmetry for all three perovskites. Fig. 3a ∼ f illustrate these variation of the composition that would be expected, after the completely relaxation. Here IFL

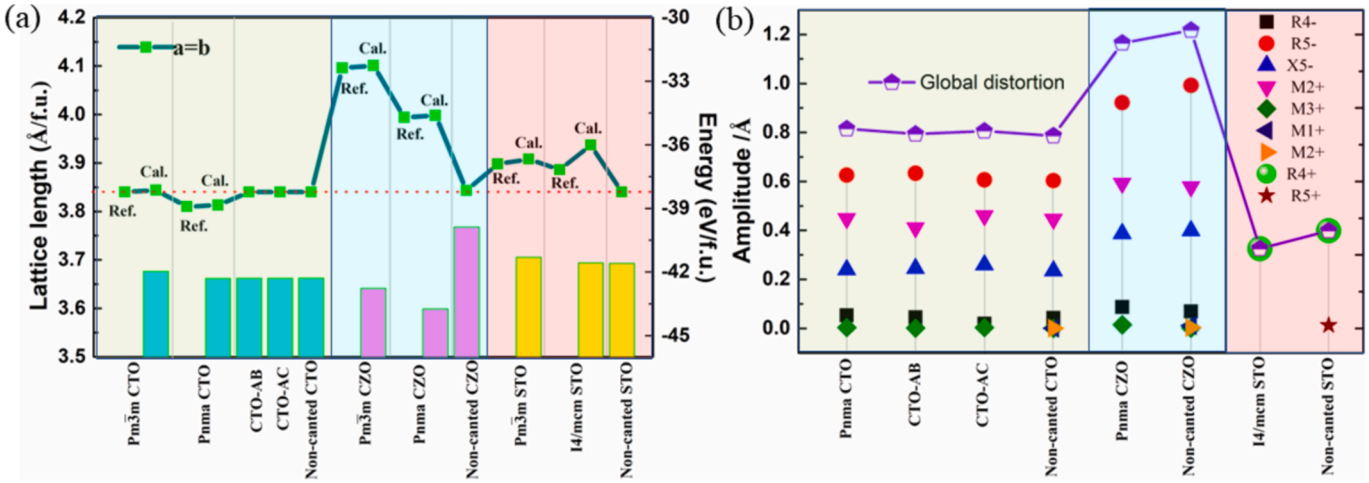

Fig. 2. (a) The comparisons of lattice parameters (Ref. 38) and total energy per formular unit in cubic, ground-state and transferred bulk perovskites; (b) The amplitude of distortion mode in non-cubic bulk perovskites, here GD refers to the total global distortion.

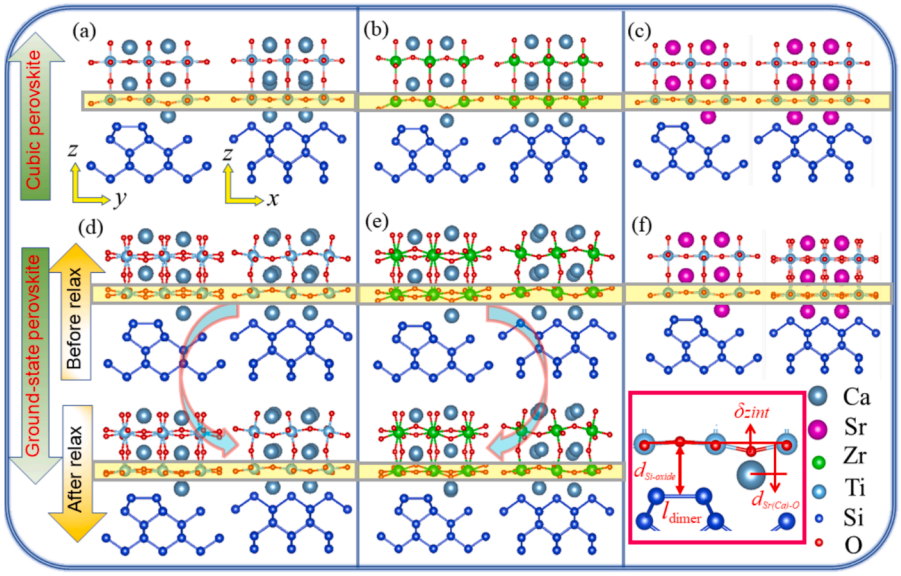

(a) 2×2×2 $Pm\bar{3}m$ $CaTiO_3 + \frac{1}{2}$ ML Ca (2A1-H)
(b) 2×2×2 $Pm\bar{3}m$ $CaZrO_3 + \frac{1}{2}$ ML Ca (2B1-H)
(c) 2×2×2 $Pm\bar{3}m$ $SrTiO_3 + \frac{1}{2}$ ML Sr (2C1-H)
(d) 2×2×2 Pnma $CaTiO_3 + \frac{1}{2}$ ML Ca (2A2-H)
(e) 2×2×2 Pnma $CaZrO_3 + \frac{1}{2}$ ML Ca (2B2-H)
(f) 2×2×2 I4/mcm $SrTiO_3 + \frac{1}{2}$ ML Sr (2C2-H)

Fig. 3. Completely relaxed heterostructures with 2 unit-cell perovskite films and half ML interfacial layer, (d) and (e) the top and the bottom parts are respectively before and after fully-relaxation in ground-state $CaTiO_3$ and $CaZrO_3$. Here the first oxide layers of perovskite film are highlighted by the yellow blocks, and the relevant distances are illustrated in inserted block, and their nomenclature as follow.

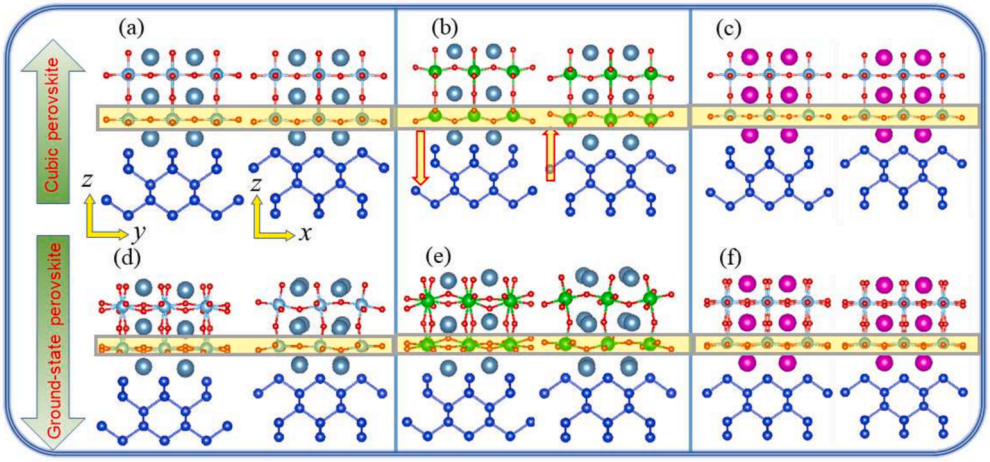

(a) 2×2×2 $Pm\bar{3}m$ $CaTiO_3$ + 1ML Ca (2A1-O)
(b) 2×2×2 $Pm\bar{3}m$ $CaZrO_3$ + 1ML Ca (2B1-O)
(c) 2×2×2 $Pm\bar{3}m$ $SrTiO_3$ + 1ML Sr (2C1-O)
(d) 2×2×2 Pnma $CaTiO_3$ + 1ML Ca (2A2-O)
(e) 2×2×2 Pnma $CaZrO_3$ + 1ML Ca (2B2-O)
(f) 2×2×2 I4/mcm $SrTiO_3$ + 1ML Sr (2C2-O)

Fig. 4. Relaxed heterostructures with 2 unit-cell perovskite films and one full ML interfacial layer, and their abbreviation as follow.

consists of half a monolayer of Ca/Sr atoms in an ordered 2 × 2 stripe pattern on the dimerized Si (001) surface. The atomic plane of the perovskites adjacent to the interface (the first oxide layer, abbreviation as FOL) is composed of TiO_2/ZrO_2 as highlighted yellow part, and Eglitis confirmed that (001) TiO_2 terminal surface in $CaTiO_3$ has weaker surface rumpling than CaO terminal surface, [45] which leads to less mismatching with Si substrate. There also gives a description of the nomenclature used with respect to these heterostructures below the pictures of these geometries.

In Fig. 3a ~ c, obviously 1/2ML Ca/Sr atoms in IFL incline to contribute two electrons out of their shell to oxygens in FOL with stronger electron affinity to form ionic bonds, rather than to the top layer of Si substrate, which finally lead into the formation of covalent Si dimers to avoid the presence of unstable Si dangling bond. Only the oxygens in FOL near Ca/Sr atoms move downwards in three cubic cases, which promote unilateral Ca/Sr cations above FOL to shift upwards to share electrons with upper perovskite layers. Inverse with $CaTiO_3$ and $CaZrO_3$, IFL Sr atoms in Fig. 3c possess bigger ionic radius and lower

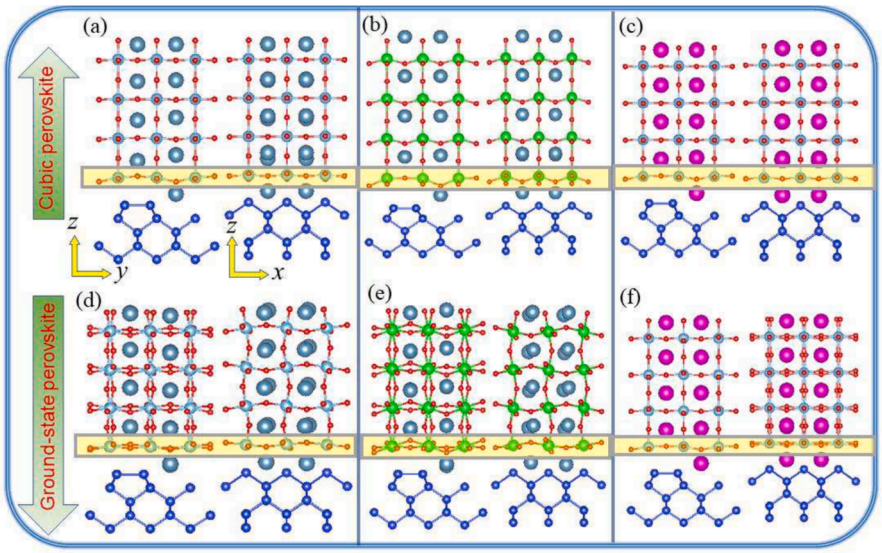

(a) 2×2×4 $Pm\bar{3}m$ $CaTiO_3 + \frac{1}{2}$ML Ca (4A1-H)
(b) 2×2×4 $Pm\bar{3}m$ $CaZrO_3 + \frac{1}{2}$ML Ca (4B1-H)
(c) 2×2×4 $Pm\bar{3}m$ $SrTiO_3 + \frac{1}{2}$ML Sr (4C1-H)
(d) 2×2×4 Pnma $CaTiO_3 + \frac{1}{2}$ML Ca (4A2-H)
(e) 2×2×4 Pnma $CaZrO_3 + \frac{1}{2}$ML Ca (4B2-H)
(f) 2×2×4 I4/mcm $SrTiO_3 + \frac{1}{2}$ML Sr (4C2-H)

Fig. 5. Relaxed heterostructures with 4 unit-cell perovskite films, and their corresponding naming convention (in parentheses).

electron affinity than Ca (Sr-1.44 Å, 74.7 KJ/mol; Ca-1.34 Å, 78.3 KJ/mol), which eventually leads to a weaker change (δ_{zint}) in the interfacial layer and upper Sr parts in perovskite film. In Fig. 3b, the unitcell of cubic $CaZrO_3$ owns larger lattice parameter (4.10 Å), and perovskite film in its heterostructure tolerates the compressive strain along (0 1 0) and (1 0 0) directions when the lattice matches with Si. It is ultimately found that oxygen atoms in whole $CaZrO_3$ film all shift along c axis to release the inner strain to keep the stability of entire structure.

Fig. 3d ~ f illustrates the variation of three ground-state perovskites in their heterostructures, here the top and the bottom parts are respectively structural models before and after fully-relaxation. The comparison of these structures indicates that the ground-state perovskite can realize the successful deposition on Si substrate without the atomic dislocation after the fully relaxation, and the influence of IFL Ca/Sr on perovskites film mainly happens on oxygens in FOL toward IFL, which reduce the amplitude of distortion in FOL.

The whole monolayers (1ML) inserted in IFL is indispensable to consider the contribution of redundant electrons on their entire geometries and electronic structures, as in Fig. 4 with a full ML of Sr/Ca. STEM images of $SrTiO_3$/Si heterostructures in relevant works indicates a full ML of Sr could be generated adjacent to the top silicon layer, through the atomic rearrangements at the interface during the growth procedure under the relatively high temperatures [9,32,46]. Obviously, the sufficient electron supply in the middle layer makes Si dimer open in all cases, which results that the perovskite films get less electrons from IFL and smaller cation-oxygen displacement ($d_{Sr(Ca)-O}$) compared with 1/2ML IFL situations in Fig. 3. While $CaZrO_3$ film in Fig. 4b shows the same oxygen movement with that in Fig. 3b.

The upper perovskite films are extended to 4 unit-cell thickness in 2 × 2 heterostructures with 1/2 IFL Sr/Ca in Fig. 5, for the sake of considering the influence of perovskite thickness. The presence of Si dimer and oxygen atoms in FOL close to IFL Ca/Si both happen in Fig. 3 and Fig. 5. In Fig. 5b, as the thickness of CZO film increases, the compressive strain exerted in CZO film caused by the lattice-mismatch could be released partly by upward transmission. This is suggested from previous PZT conclusion [47].

(2) Atom displacement around interfacial layer

Three kinds of geometrical variations are summarized in Table 1, and we separately compare the contribution of 1/2 ML and 1ML IFL on 2 unit-cell thickness geometric structures, and also the distinction of 2 and 4 unit-cell thickness of perovskite films. On the concentration comparison of IFL Ca/Sr, previous result of STO/Si reveals that electron transfer happens from the Si/Ca layers into O p orbitals and Ti d orbital in FOL, [12,33] so 1/2ML IFL transfers less electrons than 1ML IFL, and this leads to a decreased $d_{Si\text{-}oxide}$, a decreased $d_{Sr(Ca)\text{-}O}$, and then an increased δ_{zint} in 1/2ML cases (2A1-H, 2B1-H and 2C1-H). In addition, owing to the more tolerance for extra electrons from IFL atoms in perovskite films with 4 unit-cell thickness, these cases show shorter l_{dimer} from Si lack of electrons, and shorter trends of $d_{Si\text{-}oxide}$ and $d_{Sr(Ti)\text{-}O}$ same with that of 1/2ML IFL cases. Previous work suggests that the shorter silicon-oxide distance

Table 1
Key parameters from calculated geometries: oxygen displacement in the perovskite layer adjacent to the interface (δ_{zint}) in Å; the distance between the interfacial Sr (or Ca) and oxygen in the first oxide layer in perovskite ($d_{Sr(Ca)\text{-}O}$) in Å; the average distance between the top Si layer and the first oxide atomic plane of perovskite film ($d_{Si\text{-}oxide}$) in Å; the Si dimer length (l_{dimer}) in Å. Here, IFL and FOL represent for the interface layer and the first oxide layer of perovskite film.

Label	IFL	FOL	δ_{zint}	$d_{Sr(Ca)\text{-}O}$	$d_{Si\text{-}oxide}$	l_{dimer}
2A1-H	1/2 ML Ca	TiO2	0.440	2.479	2.835	2.558
2B1-H	1/2 ML Ca	ZrO2	0.499	2.294	3.065	2.538
2C1-H	1/2 ML Sr	TiO2	0.321	2.456	2.948	2.560
2A2-H	1/2 ML Ca	TiO2	0.296	2.233	2.874	2.584
2B2-H	1/2 ML Ca	ZrO2	0.327	3.051	3.026	2.682
2C2-H	1/2 ML Sr	TiO2	0.318	2.461	2.946	2.560
2A1-O	1 ML Ca	TiO2	0.246	2.508	2.967	No dimer
2B1-O	1 ML Ca	ZrO2	0.478	2.508	3.304	No dimer
2C1-O	1 ML Sr	TiO2	0.275	2.609	3.448	No dimer
2A2-O	1 ML Ca	TiO2	0.127	2.231	3.023	No dimer
2B2-O	1 ML Ca	ZrO2	0.121	2.858	3.098	No dimer
2C2-O	1 ML Sr	TiO2	0.226	2.612	3.448	No dimer
4A1-H	1/2 ML Ca	TiO2	0.432	2.269	2.825	2.547
4B1-H	1/2 ML Ca	ZrO2	0.512	2.199	3.498	2.435
4C1-H	1/2 ML Sr	TiO2	0.349	2.440	2.956	2.554
4A2-H	1/2 ML Ca	TiO2	0.535	2.225	2.829	2.588
4B2-H	1/2 ML Ca	ZrO2	0.438	3.060	3.022	2.677
4C2-H	1/2 ML Sr	TiO2	0.298	2.447	2.953	2.555

observed in the compositions with a TiO_2 FOL could increase the stability of the heterostructure, and also has a significant effect on the electronic structure [12].

(3) The electronic structure of three categories

The electronic structures in relation with heterostructures in Fig. 3 are correspondingly illustrated in Fig. 6a. From the contribution of density of states around the Fermi level, it exhibits semiconductor behavior in 2B1-H and 2B2-H systems, in contrast with the metallicity in other systems. Partial density of states (PDOS) in all cases reveal the maximum of valence band (VBM) composed of Si locates at 0.0 eV. Due to the charge transfer of IFL Ca/Sr atoms into perovskite film, the energy level of oxygen and transition metal (TM) in bulk perovskites move toward lower energy, which are normally sited around Fermi level (0.0 eV) and the minimum of conduction band (CBM) in DOS of bulk perovskites, respectively. Here oxygen and TM energy level shift roughly 2.0 eV downwards, under the consideration of gap underestimation in GGA calculation. Moreover, all DOS of a full monolayer IFL are described in Fig. 6b. It is clearly seen that four more electrons from IFL cause all energy level to shift into lower energy than 1/2 ML cases, and all cases into the metallic condition with Fermi level into conduction bands.

Different from heterostructures with 2 unit-cell perovskite film, here 4 unit-cell perovskite film in Fig. 6c show the metallicity in DOS, so 2 unit-cell film can be treated as the critical thickness. Relative works suggest that 3 unit-cell perovskite film can switch insulator into metallic transition (MIT), in modulating the conductivity of perovskite superlattice through the A-site charge modulation [48–51]. The thicker film causes the weaker film polarization, and the stronger orbital hybridization, which is identified by Si PDOS around the Fermi level in Fig. 6c. Here the energy levels of interfacial Ca atoms are specially highlighted in CZO cases (Fig. 6c-ii), since they show the clear hybridization with others, and finally produce a significant effect on the electron redistribution around the interface by the metallic behavior.

(4) The total energy of three categories

The total energy per atom of all heterostructures involved are gathered in Fig. 7a, where the dot lines separate these three categories, in manner of comparing congeneric perovskite with cubic and ground-state. The re-bonding of variant functional layers occurred in heterostructures cause the energy change different from that of bulk perovskites, but it undoubtedly follows the lower energy of heterostructures with ground-state perovskite than that of cubic ones, and thicker heterostructures obtain lower energy. Among the results, the subtle difference exits in CTO and STO cases, but as the increased thickness of perovskite films, the margin is extended obviously. On account of the larger compressive strain in CZO films, it leads to a huge effect on the energy difference in heterostructures with cubic and ground-state CZO, with the gap greater than 0.124 eV/atom and tremendously different from CZO bulks.

Band alignment in heterostructures

The band alignment with valence and conduction band offset is the most significant feature to dominate its actual application in one heterostructure based on electronic structure. The simplest method to obtain the band offset is usually achieved through assuming a common vacuum level and then acquiring the difference in their electron affinities of the two bulk materials [52]. However in fact, this simple model is inadequate to predict the accurate band offsets, due to its neglect on the effects of the interfacial chemistry, which causes the additional electron redistribution to affect electronic potential offsets. Therefore, our calculations consider this issue to predict the accurate band offsets in a complex heterosystem and the subsequent application from the electronic properties.

The computed band offsets for six perovskite/Si cases in Fig. 3 are shown schematically in Fig. 7b and compiled in Table 2, owing to their semiconductor character of two construction (2B1-H, 2B2-H). Firstly, the results in Table 2 shows that the formation of chemical bond in the interface causes a larger valence-band offset and a correspondingly smaller conduction-band offset in cubic perovskite parts. Furthermore, the results in cubic $SrTiO_3$/Si case are quite consistent with previous study through the same method ($\Delta Ev = -1.6$ eV, $\Delta Ec = 0.5$ eV) [12], which confirm the reliability of this calculation. We notice that several experimental measurements of the valence-band offset carried out on $SrTiO_3$/Si heterostructures have been reported for the comparison purpose with theoretical calculation. Among them, Amy et al. obtain valence-band offsets of 2.38 eV and 2.65 eV after two different process methods by using x-ray photoemission spectroscopy (XPS), which demonstrates the theoretical measurement shows smaller valence-band

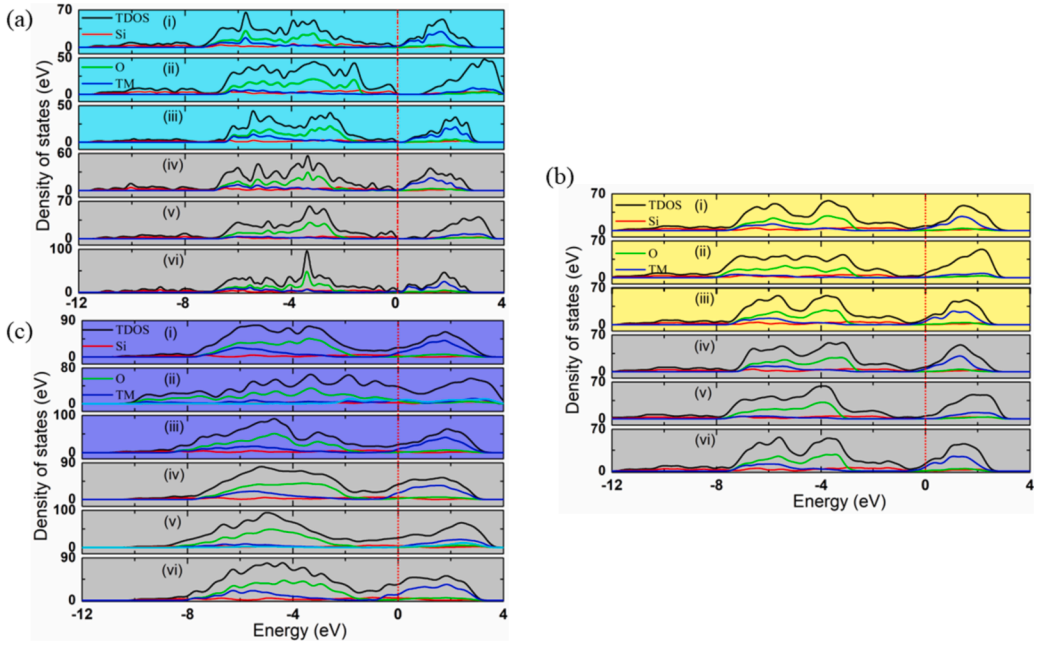

Fig. 6. Total density of states and partial density of states for (a) 2 × 2 heterostructures with 2 unit-cell perovskites and half ML interfacial layer; (b) 2 × 2 heterostructures with 2 unit-cell perovskites and one ML interfacial layer; (c) 2 × 2 heterostructures with 4 unit-cell perovskites and half ML interfacial layer.

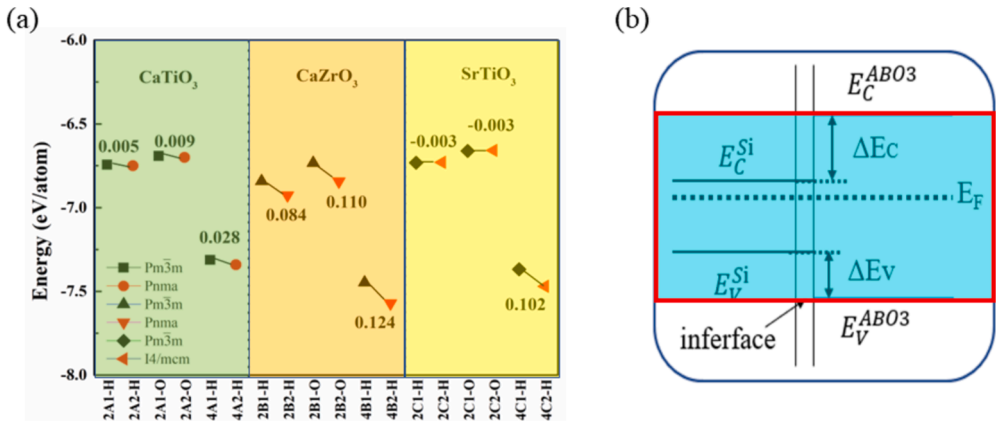

Fig. 7. (a) The comparison of total energy for all heterostructures, black and red symbols represent for cubic and ground-state perovskite film; (b) The schematic of the computed band alignment.

Table 2
Band offset for 2 × 2heterostructures with 2 unit-cell perovskites and half of ML interfacial layer, and the experimental bandgaps of six bulk perovskites, 1.12 eV experimental gap for Si.[53,54].

	Perovskite Eg/eV	ΔEv/eV	ΔEc/eV
2A1-H	3.5 [55]	−1.29	0.86
2B1-H	4.9 [56]	−3.41	0.24
2C1-H	3.25 [57,58]	−1.44	0.50
2A2-H	3.8 [59]	−0.42	2.07
2B2-H	5.7 [59]	−1.77	2.58
2C2-H	3.2 [59]	−0.89	0.99

offsets [60]. Including the typical cubic $SrTiO_3$/Si case, these six types of heterostructures all show the type-I band alignment as described in Fig. 7b [61]. Among this category, 2B2-H (Pnma $CaZrO_3$) shows excellent electrical property with larger ΔEv and ΔEc than 1.0 eV, to effectively block carrier and reduce leakage current. And this finding demonstrates that Pnma $CaZrO_3$ as the candidate of gate dielectric deserves an in-depth study.

Conclusion

In summary, this work reports a new approach of the exploitation of the alternative perovskite film in the integration with Si substrate to overcome the interfacial-unstable limitation of cubic $SrTiO_3$ in the past decades. Through first-principles calculations, firstly we demonstrate that the ground-states structures of $CaTiO_3$ and $CaZrO_3$ are performed using the effective "strained bulk" method to achieve the remarkable stability, and then the semiconductive $CaZrO_3$/Si heterostructures are obtained under the thickness of perovskite film as small as two unit-cells and half-monolayer interfacial layer. Furthermore, we find that the semiconductor behavior becomes the metallicity with the increased thickness to four unit-cells and one monolayer of interfacial atoms. The in-depth analysis provides a bright sight that the transition of electronic characteristic originates from the strong hybridization between interfacial calcium (or strontium), oxygen in the first oxide layer of perovskite and also silicon in the top layer of Si substrate, finally caused the electron redistribution in the interface. Our findings are quite general and open new perspectives for the exploitation of non-cubic and ambient-temperature phase perovskite in the integration with silicon for highly effective memory storage devices. Under the navigation in advance for the converted application of this mechanism on other perovskites, and also the synthesis of integrated heterostructures, we expect our findings will arouse subsequent experimental works on novel perovskite/Si integration materials.

CRediT authorship contribution statement

Yunting Liang: Writing – review & editing, Writing – original draft, Visualization, Validation, Supervision, Software, Resources, Project administration, Methodology, Investigation, Funding acquisition, Formal analysis, Data curation, Conceptualization. **Yajun Zhang:** Methodology, Software, Writing – review & editing. **Wenyi Tong:** Methodology, Software, Writing – review & editing. **Philippe Ghosez:** Conceptualization, Methodology, Writing – review & editing. **Eric Bousquet:** Conceptualization, Methodology, Writing – review & editing. **Matjaž Spreitzer:** Conceptualization, Methodology, Writing – review & editing.

Declaration of competing interest

The authors declare that they have no known competing financial interests or personal relationships that could have appeared to influence the work reported in this paper.

Acknowledgments

This work was financially supported by SIOX Project [M-ERA.NET 3330-17-500100], and Henan Province Science and Technology Research Projects (Grant No. 232102231001, 242300420256, 242102231036). We acknowledge access to Céci computing facilities funded by F.R.S.-FNRS Belgium [Grant No. 2.5020.1] and Tier-1 supercomputer of the Fédération Wallonie-Bruxelles funded by the Walloon Region [Grant No. 1117545].

Data availability

Data will be made available on request.

References

[1] Feldman LC, Gusev EP, Garfunkel E. Kluwer Academic Publishers, Boston, 1998.
[2] Schaller RR. IEEE Spectr 1997;34(6):52–9.
[3] Meindl JD. J Vac Sci Technol 1996;14:192.
[4] Conner J, Xie Y, Mahmut K. Microelectron Eng 1996;30(1):11–5.
[5] Basceri C, Streiffer SK, Kingon AI, Waser R. J Appl Phys 1997;82:2497.
[6] Wilk GD, Wallace RM, Anthony JM. J Appl Phys 2001;89:5243.
[7] Robertson J. Eur Phys J: Appl Phys 2004;28:265.
[8] Wolfram T and Ellialtioglu S. Cambridge University Press, Cambridge, 2006.
[9] McKee RA, Walker FJ, Chisholm MF. Phys Rev Lett 1998;81:3014.
[10] Li H. J Appl Phys 2003;93:4521.
[11] Yu HL, Wu YZ, Jiang XF. J Appl Phys 2013;114(17):173502.
[12] Kolpak AM, Beigi SI. Phys Rev B 2012;85:195318.
[13] Lee KH, Saada S, Arnault JC. Diamond Relat Mater 2016;66:67–76.
[14] Shao QY, Li AD, Cheng JB. Appl Surf Sci 2005;250(1–4):14–20.
[15] Hwang SC, Choi GM. Solid State Ion 2006;177(35–36):3099–103.
[16] Adamo C, Méchin L, Heeg T, Katz M. APL Mater 2015;3(6):062504.

[17] Braue W, Mechnich P. J Am Ceram Soc 2011:1–7.
[18] Hubbard KJ, Schlom DG. J Mater Res 1996;11(11):2757–76.
[19] Riste T, Samuelsen EJ, Otnes K. Solid State Commun 1971;9(17):1455–8.
[20] Ali R, Yashima M. J Solid State Chem 2005;178(9):2867–72.
[21] Chen F, Li YH, Gao GY. J Am Ceram Soc 2015;98(4):1372–6.
[22] Yashima M, Ali R. Solid State Ion 2009;180(2–3):120–6.
[23] Hohenberg P, Kohn W. Phys Rev 1964;136:B864–71.
[24] Kohn W, Sham LJ. Phys Rev 1965;140:A1133–8.
[25] Blöchl PE. Phys Rev B 1994;50:17953–79.
[26] Kresse G, Furthmüller J. Comput Mater Sci 1996;6:15–50.
[27] Perdew JP, Ruzsinszky A, Csonka GI, Vydrov OA. Phys Rev Lett 2008;100:136406.
[28] Monkhorst HJ, Pack JD. Phys Rev B 1976;13(12):5188.
[29] Wang J, Hallmark JA, Marshall DS, Ooms WJ. Phys Rev B 1999;60:4968–71.
[30] Först CJ, Ashman CR, Schwarz K, Blöchl PE. Nature 2004;427:53–6.
[31] Bengtsson L. Phys Rev b 1999;59:19.
[32] Mi SB, Jia CL, Vaithyanathan V, Houben L. Appl Phys Lett 2008;93:101913.
[33] Garrity K, Ismail-Beigi S. Phys Rev B 2009;80:085306.
[34] Forst CJ, Ashman CR, Schwarz K, Blochl PE. Nature 2003;427:53.
[35] Van de Walle CG, Martin RM. Phys Rev B 1987;35:8154–65.
[36] Conesa JC. J Phys Chem C 2012;116:18884–90.
[37] Paasch G, von Faber E. Prog Surf Sci 1990;35:19–33.
[38] Xiao H, Goddard WA. J Chem Phys 2014;141:094701.
[39] Eglitis RI, Jia R. Materials 2023;16:7623.
[40] Amoroso D, Cano A, Ghosez P. Phys Rev B 2018;97(17):174108.1–174108.24.
[41] Eklynd CJ, Fennie CJ, Rabe KM. Phys Rev 2009;79(22):220101.1–4.
[42] Zayak AT, Huang X, Neaton JB, Rabe KM. Phys Rev B 2006;74:094104.
[43] Potocnik TP, Zupanic E, Tong WY. Appl Surf Sci 2019;471:664–9.
[44] Segal Y, Reiner JW, Kolpak AM. Phys Rev Lett 2009;102:116101.
[45] Eglitis RI, Vanderbilt D. Phys Rev B 2008;78:155420.
[46] Kolpak AM, Walker FJ, Reiner JW, Segal Y. Phys Rev Lett 2010;105:217601.
[47] Liu G, Nan CW. J Phys d: Appl Phys 2005;38:584.
[48] Kalisky B, Bert JA, Klopfer BB. Nat Commun 2012;3(6):922.
[49] Biswas A, Kim KS, Jeong YH. J Appl Phys 2014;116(21):226402.
[50] Ohtomo A, Muller DA, Grazul JL. Nature 2002;419(6905):378–80.
[51] Takizawa M, Tsuda S, Susaki T. Phys Rev B: Condens Matter 2011.
[52] Wagner S. Microelectron J 1982.
[53] Gryko J, Mcmillan PF, Marzke RF. Phys Rev B 2000;62(12):R7707–10.
[54] Ranjan V, Kapoor M, Singh VA. J Phys: Condens Matter 2001;14:26.
[55] Saha S, Sinha TP, Mookerjee A. Eur Phys J B 2000;18(2):207–14.
[56] Rosa LV, Oliveira MC, Assis M. Ceram Int 2015;41(2):3069–74.
[57] Benthem KV, Elssser C, French RH. J Appl Phys 2001;90:12.
[58] Mitra C, Lin C, Robertson J. Phys Rev B 2012;86(155105):755–9.
[59] Krause A, Weber WM, Pohl D. J Phys D: Appl Phys 2015;48(41):415304.
[60] Amy F, Wan AS, Kahn A, Walker FJ, Mckee RA. J Appl Phys 2004;96:1635.
[61] Tiwari S, Kumar A, Welser JJ. Int J High Speed Electron Syst 2000;10(01):231–45.